The 15 February 2014 M_w 4.1 South Carolina Earthquake Sequence: Aftershock Productivity, Hypocentral Depths, and Stress Drops

Clara Daniels[1*], Zhigang Peng[1], Qimin Wu[2], Sidao Ni[3], Xiaofeng Meng[4], Dongdong Yao[5], Lara S. Wagner[6], and Karen M. Fischer[7]

Abstract

The border between Georgia and South Carolina has a moderate amount of seismicity typical of the Piedmont Province of the eastern United States and greater than most other intraplate regions. Historical records suggest on average a M_w 4.5 earthquake every 50 yr in the region of the J. Strom Thurmond Reservoir, which is located on the border between Georgia and South Carolina. The M_w 4.1 earthquake on 15 February 2014 near Edgefield, South Carolina, was one of the largest events in this region recorded by nearby modern seismometers, providing an opportunity to study its source properties and aftershock productivity. Using the waveforms of the M_w 4.1 mainshock and the only cataloged M_w 3.0 aftershock as templates, we apply a matched-filter technique to search for additional events between 8 and 22 February 2014. The resulting six new detections are further employed as new templates to scan for more events. Repeating the waveform-matching method with new templates yields 13 additional events, for a total of 19 previously unidentified events with magnitude 0.06 and larger. The low number of events suggests that this sequence is deficient in aftershock production, as compared with expected aftershock productivities for other mainshocks of similar magnitudes. Hypocentral depths of the M_w 4.1 mainshock and M_w 3.0 aftershock are estimated by examining the differential time between a depth phase called *sPL* and *P*-wave arrivals, as well as by modeling the depth phase of body waves at shorter periods. The best-fitting depths for both events are around 3–4 km. The obtained stress drops for the M_w 4.1 mainshock and M_w 3.0 aftershock are 3.75 and 4.44 MPa, respectively. The corresponding updated moment magnitude for the aftershock is 2.91.

Cite this article as Daniels, C., Z. Peng, Q. Wu, S. Ni, X. Meng, D. Yao, L. S. Wagner, and K. M. Fischer (2019). The 15 February 2014 M_w 4.1 South Carolina Earthquake Sequence: Aftershock Productivity, Hypocentral Depths, and Stress Drops, *Seismol. Res. Lett.* **91**, 452–464, doi: 10.1785/0220190034.

Introduction

Seismicity in the Piedmont region of Georgia and South Carolina is characterized by shallow depths of less than 5 km, small clusters, and local magnitudes typically less than 4 (e.g., Long, 2009). The major epicentral zones are near Lake Sinclair in central Georgia, the J. Strom Thurmond Reservoir at the border between Georgia and South Carolina, and reservoir-induced seismicity near the Lake Jocassee and Monticello Reservoir areas (Bollinger *et al.*, 1991). Most earthquakes are single, isolated events except for concentrations of epicenters in the vicinity of reservoirs (Long, 2009) or major rivers (Costain, 2008).

On 15 February 2014 at 3:23:38 UTC (14 February 2014 10:23:38 EST), an earthquake occurred near Edgefield, South Carolina (Fig. 1). The U.S. Geological Survey's (USGS's) National Earthquake Information Center (NEIC) catalog listed the moment magnitude (M_w) as 4.1. The epicenter (33.817° N,

1. School of Earth and Atmospheric Sciences, Georgia Institute of Technology, Atlanta, Georgia, U.S.A.; 2. School of Geology and Geophysics, The University of Oklahoma, Norman, Oklahoma, U.S.A.; 3. Institute of Geodesy and Geophysics, Chinese Academy of Sciences, Wuhan, China; 4. Department of Earth Sciences, University of Southern California, Los Angeles, California, U.S.A.; 5. Earth and Environmental Sciences, University of Michigan, Ann Arbor, Michigan, U.S.A.; 6. Department of Terrestrial Magnetism, Carnegie Institution for Science, Washington, D.C., U.S.A.; 7. Department of Earth, Environmental and Planetary Sciences, Brown University, Providence, Rhode Island, U.S.A.

*Corresponding author: cdaniels9@gatech.edu

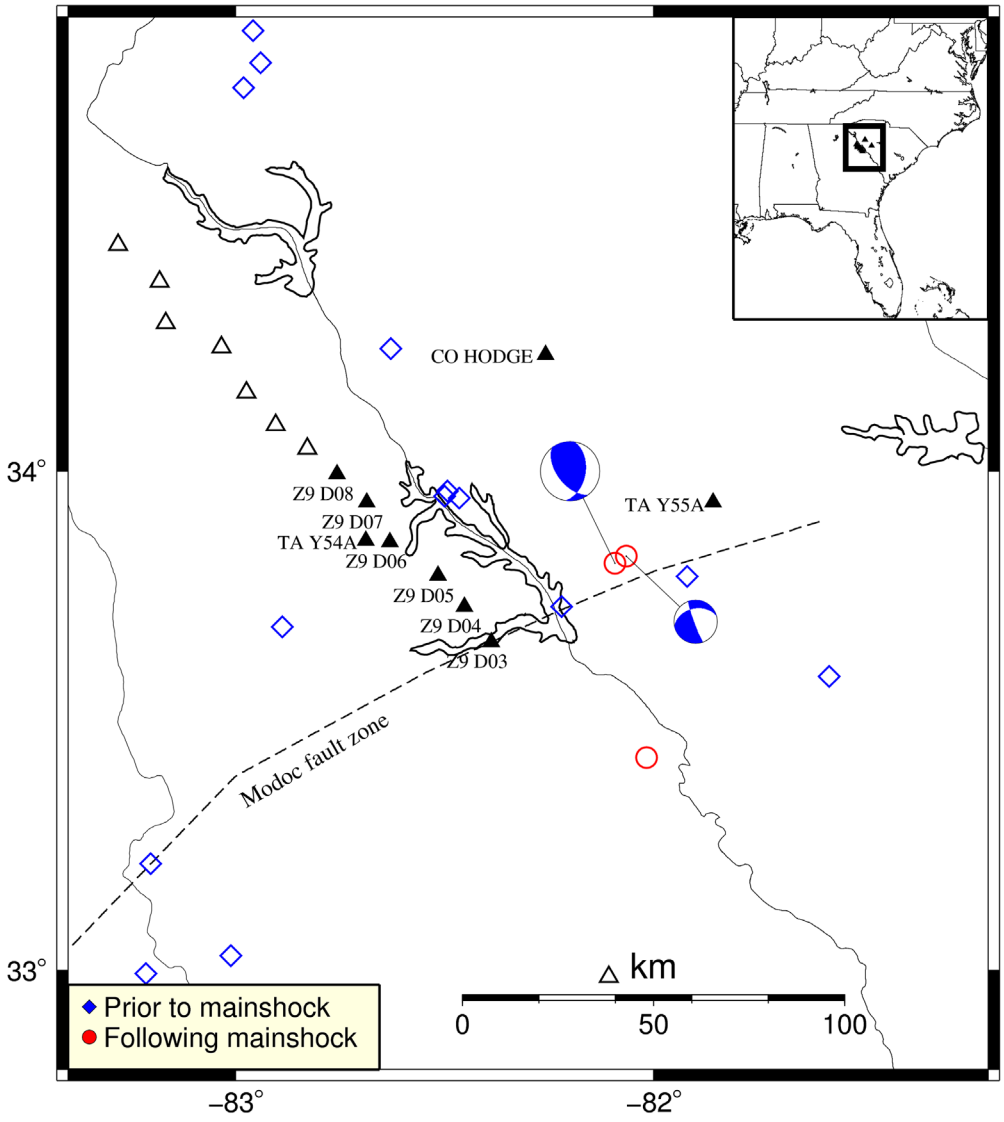

Figure 1. Map of study region around the 2014 M_w 4.1 mainshock on 15 February 2014 at 3:23:38 UTC. Solid triangles indicate the nine stations used to perform final detections for missing events from the Advanced National Seismic System (ANSS) catalog. Empty triangles indicate available Z9 stations not used in the analysis. Diamonds correspond to background events with magnitude greater than or equal to 3 since 1970 that occurred prior to the mainshock, whereas circles correspond to those that occurred following the mainshock. The focal mechanisms for the M_w 4.1 mainshock and M_w 3.0 aftershock are also plotted. The location of the 1974 M_L 4.3 earthquake is also indicated. The Modoc fault zone is shown as the dashed line. The inset shows the location of the study area within the Southeast United States. The color version of this figure is available only in the electronic edition.

82.092° W with a precision of 0.6 km, according to the USGS) was close to the state border of Georgia and South Carolina and was widely felt in both states. According to the USGS's "Did You Feel It?" webpage, vibrations were felt to a distance of ~300 km with a maximum intensity of V (moderate) on the modified Mercalli intensity scale.

The epicenter is about 20 km to the east of the Thurmond Reservoir (known as the Clarks Hill Reservoir in Georgia) and about 30 km northwest of Augusta, Georgia. The M_w 4.1 mainshock was followed by an M_w 3.0 aftershock on 16 February at 20:23:35 UTC. However, no additional earthquakes were reported around the time of the mainshock. The USGS's NEIC catalog listed the depth of the M_w 4.1 mainshock as 5.18 ± 0.8 km and the depth of the M_w 3.0 aftershock as 6.99 ± 1 km. Other reported solutions include a depth of 5 km by St. Louis University (SLU) and the USGS's moment-tensor (MT) depth of 6 km for the mainshock (see Data and Resources). This sequence was recorded by several stations in the region, the closest of which is 25.4 km from the epicenter. Permanent stations within 48 km include CO HODGE and CO HAW. There was also a temporary seismic network named Southeastern Suture of the Appalachian Margin Experiment (SESAME) (network code: Z9; Fischer *et al.*, 2010). The nearby Modoc fault zone is also shown in Figure 1.

In this study, we conduct a systematic investigation of the source properties (i.e., hypocentral depths, stress drops, and so on) of the M_w 4.1 mainshock and M_w 3.0 aftershock. To determine whether there are missing events around the mainshock, we apply a matched-filter technique (Peng and Zhao, 2009) to scan through continuous waveforms to detect additional events covering the time period of 8–22 February 2014. More accurate depths of these two events are estimated by examining the differential time between a particular depth phase called *sPL* (Chong *et al.*, 2010) and *P*-wave arrivals. The stress drop for the M_w 4.1 mainshock and its M_w 3.0 aftershock are determined by the multiwindow coda spectral ratio (MWCSR) method (Wu and Chapman, 2017). An updated seismic moment of the

aftershock is calculated by computing the moment difference relative to the mainshock.

Previous Studies and Seismic Data

Previous studies on earthquakes in the Piedmont Province of Georgia and South Carolina suggest that earthquakes near the Thurmond Reservoir occur on smooth, lubricated faults with low normal stress and multiple plane orientations, which may correspond to different joints in the rock (Guinn, 1977; Johnston, 1980; Marion and Long, 1980). The last earthquake with magnitude greater than 4 near this reservoir is the 2 August 1974 M_L 4.3 earthquake, and the corresponding stress drop is 1.2–12 bars (or 0.12–1.2 MPa), depending on which method is used (Bridges, 1975). This event occurred about 37 km from the 2014 mainshock and was located on the north side of the Thurmond Reservoir (Fig. 1). Furthermore, the large *b*-value in the Gutenberg–Richter (G-R) relation for earthquakes in this region and other reservoirs suggests that many smaller magnitude earthquakes are triggered due to effects of reservoir impoundment (Gupta *et al.*, 1972). The swarm behavior of these earthquakes can likely be explained through the triggering mechanism of decreased fracture or joint strength in the rock due to weathering or increased water pressure in a joint (Long, 2009). In particular, an asperity may fail by changes in hydrostatic pressure from a nearby reservoir, or lithostatic pressure and fault movement. When one asperity fails, fluids flow away from the failed joint and cause reduced strength in surrounding joints and fractures through increased fluid pressure (Long, 2019).

A plot of the background seismicity in the Thurmond Reservoir region (defined as events within 100 km of the epicenter of the M_w 4.1 mainshock) from the Advanced National Seismic System (ANSS) catalog is given in Figure 2. From 2010 to 2015, there are few events in general, with 2010 being an unusually quiet year and 2013 a comparatively seismically active year. The cluster of events in location and time from 7 to 27 April 2013 may correspond to an earthquake swarm located 25–40 km west of mainshock. However, there are no cataloged events since 2010 within 10 km of the mainshock epicenter, as well as within several months following the mainshock, aside from the M_w 3.0 aftershock. The 2 yr (2015 and 2016) following the M_w 4.1 event are relatively quiet compared with the background levels of seismicity. Among them, no events were reported in the region in 2016. It is unlikely that these detections are quarry blasts, because their times of day are mainly in the very early hours of the day or randomly throughout the day, with no peak near 8 a.m., 12 p.m., or 5 p.m., which are typical for quarry blasts in this region (T. Long, personal comm., 2019).

Figure 1 marks nearby seismic stations in the study region, including those in the temporary SESAME experiment Z9 (Parker *et al.*, 2013, 2016; Hopper *et al.*, 2017; see Data and Resources). A spectrogram from a nearby station Z9.D03 is

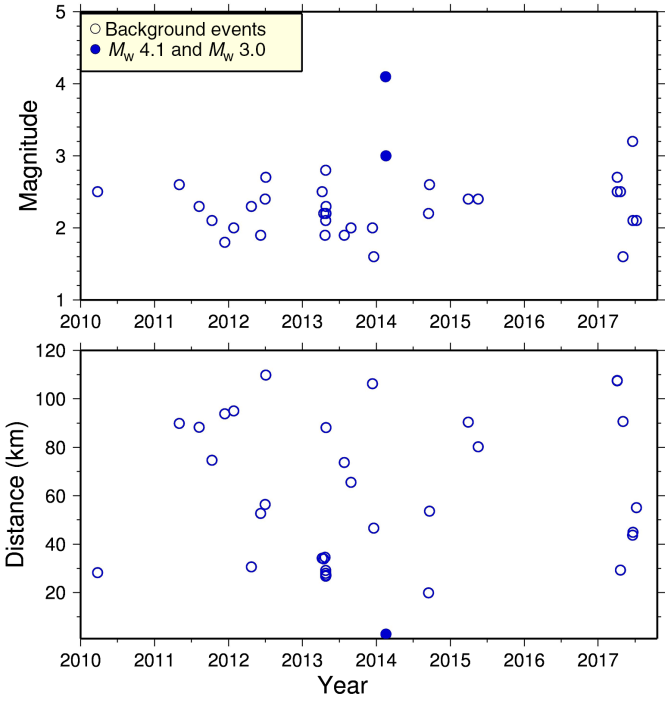

Figure 2. Background events from 1 January 2010 to 1 August 2017 in the region within ~100 km of the M_w 4.1 mainshock epicenter. The plot illustrates the magnitude and distance from the mainshock epicenter plotted against year. Solid points represent ANSS events used as templates, whereas unfilled points correspond to other recorded ANSS events. The color version of this figure is available only in the electronic edition.

shown in Figure 3. The spectrogram indicates that additional earthquakes temporally associated with the main event are not listed in the USGS catalog, motivating us to detect them with the matched-filter technique. In this study, continuous waveforms from nine stations within 100 km of the epicenter are used, including; Y55, D03, D04, D05, D06, HODGE, Y54, D07, and D08. Stations farther in distance from the mainshock epicenter have relatively lower signal-to-noise ratios (SNRs), especially for small-magnitude events.

Detection of Aftershocks Using Matched-Filter Technique

We download seismic data from the Incorporated Research Institutions for Seismology Data Management Center. A 2–16 Hz band-pass filter is applied to the continuous three-component broadband seismogram data between 8 and 22 February 2014, as this filter provides the clearest signals for local earthquakes recorded at most stations. We also resample the continuous data to 40 sample/s to speed up the matched-filter computation, as well as keeping enough high frequencies to distinguish events at short distances.

The two template events used first are the M_w 4.1 mainshock and M_w 3.0 aftershock listed in the ANSS catalog.

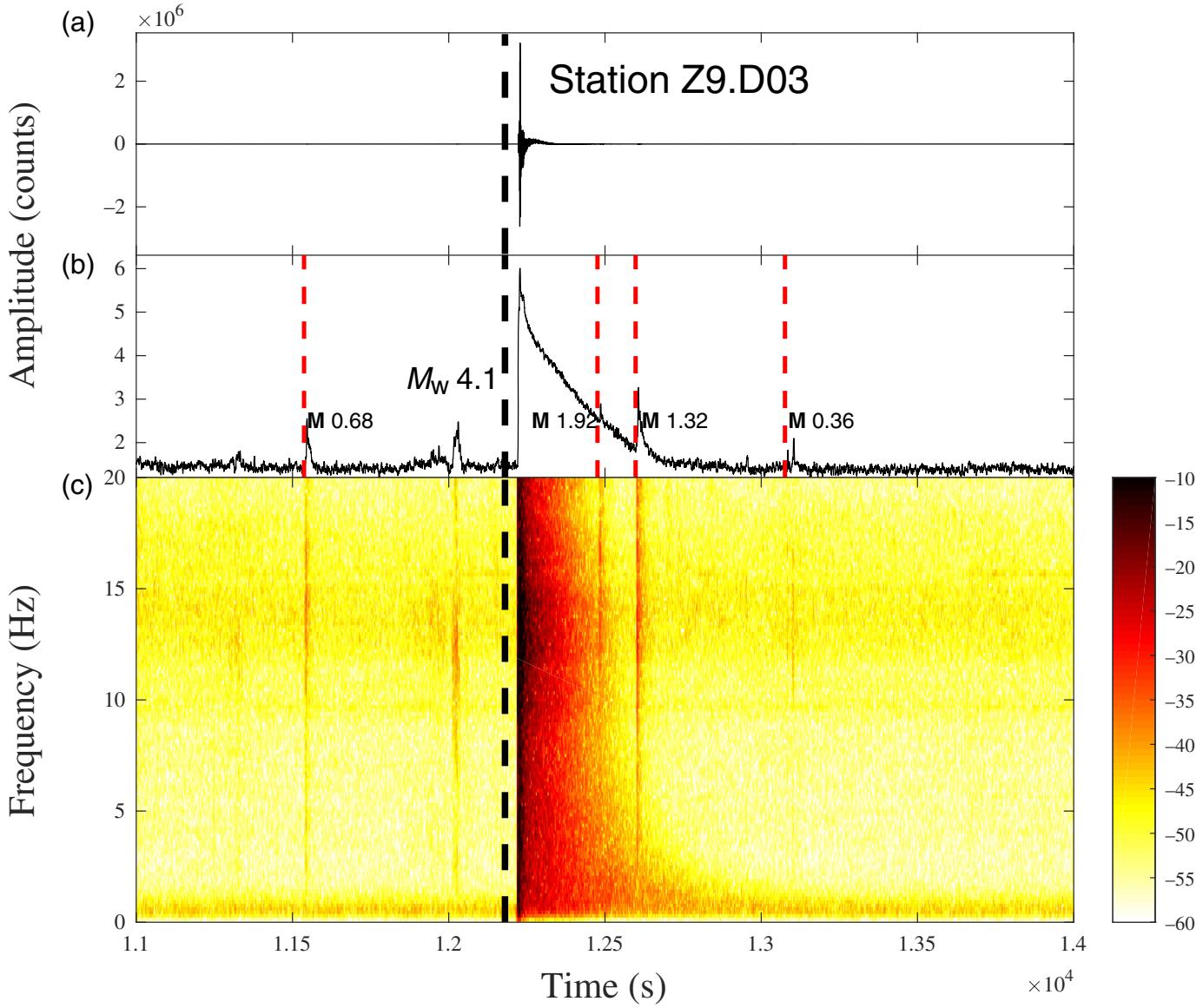

Template waveforms are cut from the continuous waveforms starting from 30 s before to 2 min after the event. *P*- and *S*-wave arrival times are manually picked by visual inspection for each waveform.

The matched-filter method only uses template waveforms that have 12 or more channels with SNR greater than 5. To compute the SNR, the signal window spans 6 s (1 s before to 5 s after) around the *P* and *S* arrivals. The noise window contains the 6 s of signal ending 1 s before the *P*-wave arrival. The sliding-window cross-correlation (CC) function is computed by shifting every 0.025 s (i.e., one sample per step). The time window for computing the CC function is set to be 1 s before to 5 s after the *P*-arrival time, and 1 s before to 5 s after the *S*-arrival time, which should provide long enough waveform segments to capture the majority of the targeted *P* and *S* waves. For vertical channels, the *P*-wave time window is used, whereas for the two horizontal channels the *S*-wave time window is used.

Figure 3. (a) Raw vertical-component seismogram recorded at station Z9.D03 showing the 2014 M_w 4.1 mainshock. The bold dashed line denotes the origin time of the mainshock. (b) Log_{10}-based 2–16 Hz band-pass-filtered envelope function showing possible foreshocks and aftershocks. Those marked by dashed lines with magnitudes marked are events detected by the template-matching method. (c) The corresponding spectrogram. The color version of this figure is available only in the electronic edition.

Individual CC functions of all channels for each day are then stacked directly, resulting in one mean trace for each continuous day. The initial threshold value for a positive detection is equal to the median plus nine times the median absolute deviation (MAD) of the mean CC trace (Shelly *et al.*, 2007).

To avoid overcounting events, duplicate detections are removed corresponding to multiple detections of the same target event with different template events (e.g., Meng *et al.*, 2013). If

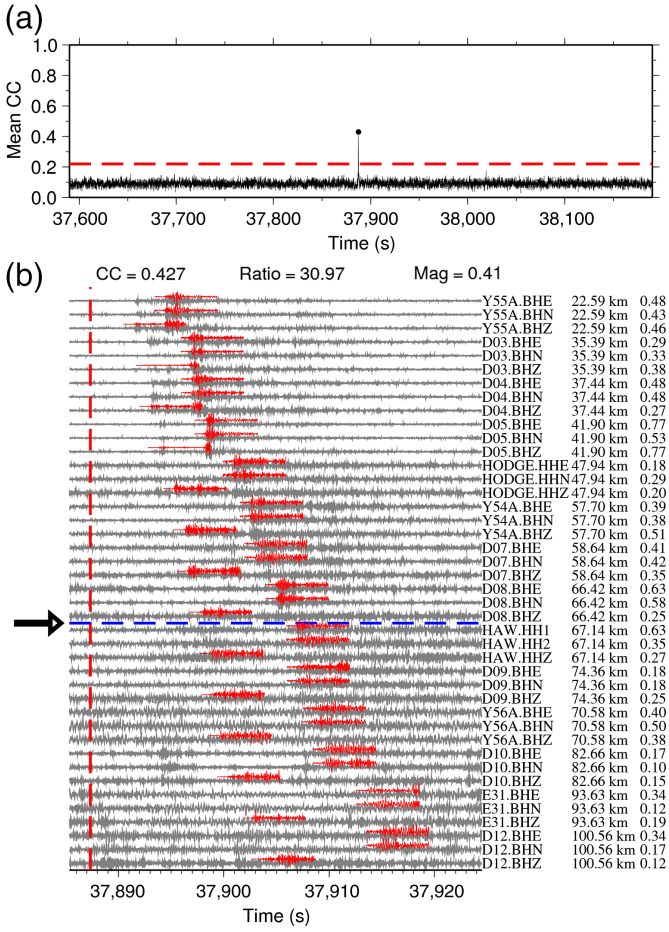

Figure 4. Example of a detected **M** 0.41 aftershock using the **M** 3.0 aftershock as a template. (a) Mean cross-correlation (CC) values around the time of the detected events. The dashed line marks the detection threshold of nine times the median absolute deviation. (b) A comparison between the 2–16 Hz continuous waveforms and the template waveforms. The continuous waveform is cut near the origin time of the detected event, which is represented by a vertical dashed line. Station names are given in the first column on the right side of the waveforms. CC values for each station are given in the second column, and approximate distances in kilometers from the detected event are given in the third column. The horizontal dashed line separates the stations used for stacking (above) from the stations not used (below). The color version of this figure is available only in the electronic edition.

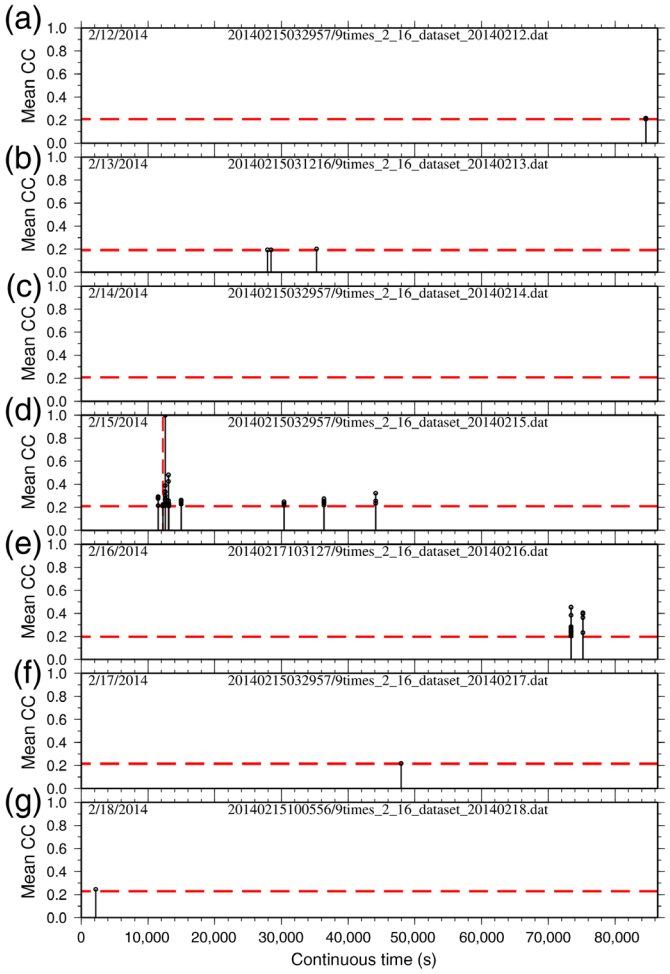

Figure 5. Mean CC values of all detections by the template marked on the top of each plot (20140215100556 M_w 4.1, 20140217103127 M_w 3.0). (a–g) The date of each panel ranges between 12 February and 18 February 2014. The threshold of nine times the median absolute deviation (MAD) added to the median CC waveform value is depicted by a dashed line on each plot. The vertical dashed line in (d) indicates the time of the mainshock on 15 February 2014. The color version of this figure is available only in the electronic edition.

there are multiple detections within 2 s of one another, only the detection with the highest CC value is kept. To obtain an approximation of the magnitude of the detected events, the median peak amplitude ratio between each detected event and its best-matched template across all channels is calculated (Peng and Zhao, 2009).

Figure 4 shows an example of a newly detected magnitude 0.41 aftershock based on the matched-filter method. The template event is the M_w 3.0 aftershock. The mean CC value for this detection is 0.427, much higher than the detection threshold of ~0.2. By visual inspection, there does indeed appear to be an event at the detected time. Stations HAW through D12 do not show the event as clearly as stations Y55A through D08, so it is more difficult to manually pick the arrival of the event for stations after D08.

The arrow and the horizontal line in Figure 4 separates the nine used stations (above the line), from those unused (below the line). For the nine stations included in this study, the event can be seen clearly and the CC values are high. For stations not included in this study, the CC values are generally low, and the event is not picked up well at these stations with distances greater than 65 km from the mainshock.

As relatively fewer events are detected with the first two templates, the detections are used in turn as new templates. The same matched-filter method is used with the new

TABLE 1
Event Detections Listed with Origin Time (UTC), Estimated Magnitude, and Mean Cross-Correlation (CC) Value

Event Origin Time (UTC) (yyyy/mm/dd hh:mm:ss.ss)	Magnitude	Mean CC
2014/02/10 00:38:37.30	0.45	0.216
2014/02/12 23:30:07.500	0.57	0.218
2014/02/13 06:05:58.200	0.41	0.21
2014/02/13 07:45:19.680	0.34	0.194
2014/02/13 07:54:11.530	0.22	0.194
2014/02/13 09:47:50.300	0.16	0.203
2014/02/14 05:51:05.80	0.06	0.188
2014/02/15 03:12:16.580	0.68	0.311
2014/02/15 03:23:38.120	4.1	1
2014/02/15 03:27:56.620	1.92	0.297
2014/02/15 03:29:57.80	0.92	0.191
2014/02/15 03:37:56.230	0.36	0.482
2014/02/15 04:09:31.920	0.56	0.263
2014/02/15 08:26:32.600	0.61	0.276
2014/02/15 10:05:56.800	0.78	0.302
2014/02/15 12:15:46.780	0.85	0.323
2014/02/16 20:23:35.770	3.0	1
2014/02/16 20:52:50.750	0.18	0.378
2014/02/17 10:31:27.350	0.41	0.427
2014/02/17 13:19:08.980	0.73	0.219
2014/02/18 00:36:30.900	0.57	0.246

templates. In summary, there are six new events found using the first two templates (the M_w 4.1 mainshock and the M_w 3.0 aftershock), as well as 13 more found using the detections as templates, for a total of 19 detections (Table 1). Figure 5 gives the mean CC values of all detections by the templates at the top of each plot, without removing multiple detections within a 2 s window.

Figure 6a shows that seven of the eight events before the mainshock are considered as positive ones only if the threshold is between 9 and 12 times the MAD. This suggests that most of the detections would not be considered as true events if a higher threshold were chosen. Hence, it is debatable whether their waveforms contain true events. The only **M** 0.68 foreshock with a relatively high mean CC value (0.311, or 19.78 times the MAD) occurred about 11 hr before the mainshock.

Using the nine times MAD threshold, there are also new 11 aftershock detections. Four of these events occurred after the M_w 3.0 event (and hence could be considered as its secondary aftershocks), and most of the aftershocks occur on the same day as the mainshock. As shown in Figure 6a, several aftershocks are persistent even with the highest threshold of 15 times the MAD, suggesting that they are likely true events. Two of the aftershocks of the M_w 3.0 event have among the highest CC coefficients among all detections, despite their low magnitudes.

Figure 6b plots the magnitude–frequency distributions for all detected events. If we exclude the M_w 4.1 mainshock and compute the G-R statistics for all detected earthquakes in the sequence around the epicentral region, the resulting a-value is 1.2 (based on the maximum-likelihood estimate). The a-value is the $\log_{10}$ of the expected number of events with magnitude >0 in a given time interval and area, and hence reflects the productivity in this region. Cumulatively, there are only 20 events with magnitudes larger than 0 other than the mainshock during our study period.

Stress-Drop Estimates

Next, we apply the MWCSR method (Wu and Chapman, 2017) to obtain corner-frequency and stress-drop estimates for the 2014 M_w 4.1 mainshock and its M_w 3.0 aftershock. This method takes advantages of the multiwindow spectral ratio method (Imanishi and Ellsworth, 2006) and the averaging property of the *S*-wave coda (Mayeda *et al.*, 2007; Somei *et al.*, 2014; Frankel, 2015; Wu *et al.*, 2016), and has shown to produce more stable spectral ratios compared with conventional empirical Green's function (EGF) or spectral ratio methods (Wu and Chapman, 2017; Wu *et al.*, 2018). The M_w 3.0 aftershock is considered as the EGF of the mainshock and the procedures of Wu and Chapman (2017) are followed to process the data.

The chosen coda window begins at twice the *S*-wave travel time and the entire coda window length is set to 30 s. The entire coda window is then divided into five successive 10-second-long subwindows overlapped by half the subwindow duration (Fig. 7a). Qualified traces from all stations within 250 km are selected by examining the common decay characteristics of coda envelopes in the entire analyzed coda window over a broad frequency range (1–2, 2–4, 4–8, and 8–16 Hz) for this mainshock–aftershock pair (Fig. 7b). The mean and standard deviation of the normalized envelope amplitude ratio (smoothed using a 10 s moving window) are required to be within 1.0 ± 0.1 and less than 0.05, respectively, and only traces that meet the criteria are accepted. This selection scheme ensures that the coda waves decay in a nearly identical manner for the event pair, indicating very similar propagation and site effects. Therefore, taking the spectral ratio of qualified traces would remove the common propagation and site effects effectively, leaving an estimate of the source spectral ratio, which can then be modeled with an assumed source spectral model (e.g., Brune, 1970, 1971; Boatwright, 1980).

The spectra of the pre-*P* noise window, the direct *S*-wave window, and the coda subwindows are calculated using a

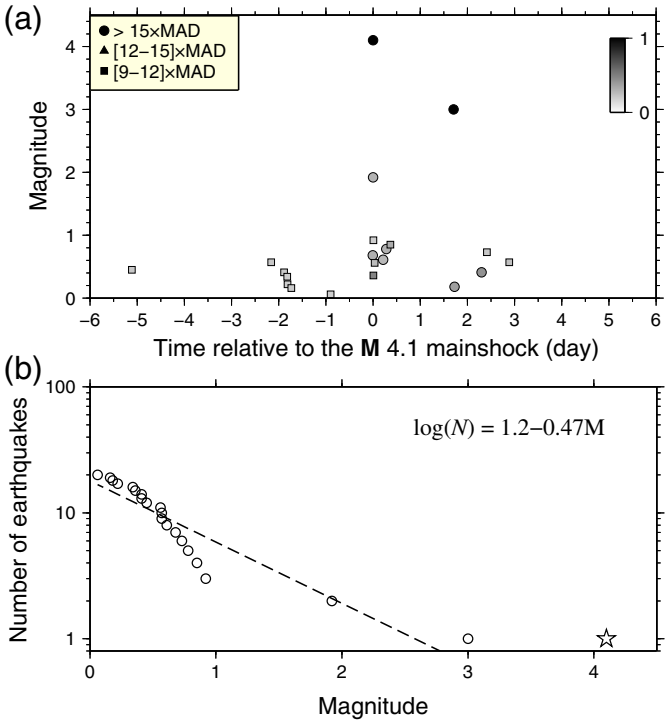

Figure 6. Distribution of two catalog events and newly detected events. (a) Magnitude of the events is plotted against time relative to the mainshock, in days. The gray scale of the data points corresponds to CC values of the events. The two template events are thus colored black, and the resulting detections have varying CC values. Detections are categorized based on the threshold level for detection used. Circular data points represent events that are detected at the highest threshold, 15 times the MAD added to the median. Triangular data points, of which there are none, represent events detected at a threshold between the range of 12–15 times MAD plus the median. Square data points represent events detected at the lowest threshold in the range of 9–12 times MAD plus the median. (b) Cumulative number of events with a magnitude above a certain level, for all events detected excluding the mainshock. The dotted line represents the best-fitting Gutenberg–Richter relationship between expected earthquake magnitude and cumulative number of events. The star represents the magnitude 4.1 mainshock in comparison to other events. The line fit represents an *a*-value of 1.2, and a *b*-value of 0.47. The color version of this figure is available only in the electronic edition.

multitaper approach (Prieto *et al.*, 2009). First, the coda spectral ratios from the five subwindows are stacked, and then the spectral ratios for all qualified traces are stacked. The spectral ratios are resampled equally in the logarithmic domain to ensure equal weights at low and high frequencies, and the SNR threshold is set at 3. For comparison, the spectral ratios for the direct *S*-wave window are also calculated (Fig. 8a, left panel). It is obvious that the spectral ratios derived from the multiwindow coda waves show less scatter across stations compared with those from the direct *S* waves (Fig. 8a). Subsequently, the stacked spectral ratios are modeled with the Brune source model (Brune, 1970, 1971)

$$\frac{u_1(f)}{u_2(f)} = \frac{M_{01}}{M_{02}} \frac{\left(1+\frac{f}{f_{c2}}\right)^2}{\left(1+\frac{f}{f_{c1}}\right)^2} = M_{\text{ratio}} \frac{\left(1+\frac{f}{f_{c2}}\right)^2}{\left(1+\frac{f}{f_{c1}}\right)^2}, \quad (1)$$

in which M_{ratio} is the ratio of the seismic moment of the two events; f_{c1} and f_{c2} are the corner frequencies of the mainshock and the aftershock, respectively. The two corner frequencies and M_{ratio} are found simultaneously using a Markov chain Monte Carlo algorithm (Salvatier *et al.*, 2016). The best estimates and uncertainties (95% confidence intervals) are determined from the posterior probability distributions (Fig. 8c). The obtained corner frequencies for the mainshock and the aftershock are 2.18 Hz (1.86–2.55 Hz, 95% confidence interval) and 9.19 Hz (8.01–10.55 Hz, 95% confidence interval).

The stress drop is then calculated from seismic moment M_0 and corner frequency f_c, assuming a circular crack model and Brune's model parameters (Eshelby, 1957; Brune, 1970, 1971).

$$\Delta\sigma = \frac{7}{16}\frac{M_0}{r^3} = \frac{7M_0}{16}\left(\frac{f_c}{k\beta}\right)^3, \quad (2)$$

$$r = \frac{k\beta}{f_c}, \quad (3)$$

in which r is the source radius, β is the shear-wave velocity at the source, which is assumed as 3.5 km/s, and κ is a constant corresponding to the specific source model (0.372 for the Brune model). The seismic moment of the mainshock is taken from SLU Earthquake Center regional MT solutions (see Data and Resources), whereas that of the aftershock is calibrated through the fitted M_{ratio}, as the MT inversion tends to have large uncertainties for small earthquakes.

The updated M_w for the aftershock is 2.91 ± 0.05, slightly lower than that from the MT solution (M_w 3.02). The stress drop of the mainshock is 3.75 MPa with a 95% confidence interval of 2.36–6.01 MPa, which is low in the context of eastern North America, where moderate-size earthquakes generally have high stress drops with typical values of ~10 MPa (e.g., Shi *et al.*, 1998; Viegas *et al.*, 2010; Boatwright and Seekins, 2011; Viegas, 2012; Wu and Chapman, 2017, and references therein). For the aftershock, this approach yields a stress drop of 4.44 MPa with a 95% confidence interval of 2.95–6.73 MPa (or 6.54 MPa with a 95% confidence interval of 4.34–9.90 MPa if M_w 3.02 is applied).

Constraints on Depth

The focal plane solution of the M_w 4.1 mainshock is resolved via inversion of full waveforms filtered between 0.02 and 0.1 Hz by the SLU earthquake center. The inversion reported a focal depth of 5 (SLU solution) and 6 km (USGS-MT). To further constrain the depth, the depth phases of body waves up to 2 Hz are modeled by comparing the observed and synthetic seismograms. Three-component raw seismograms of the

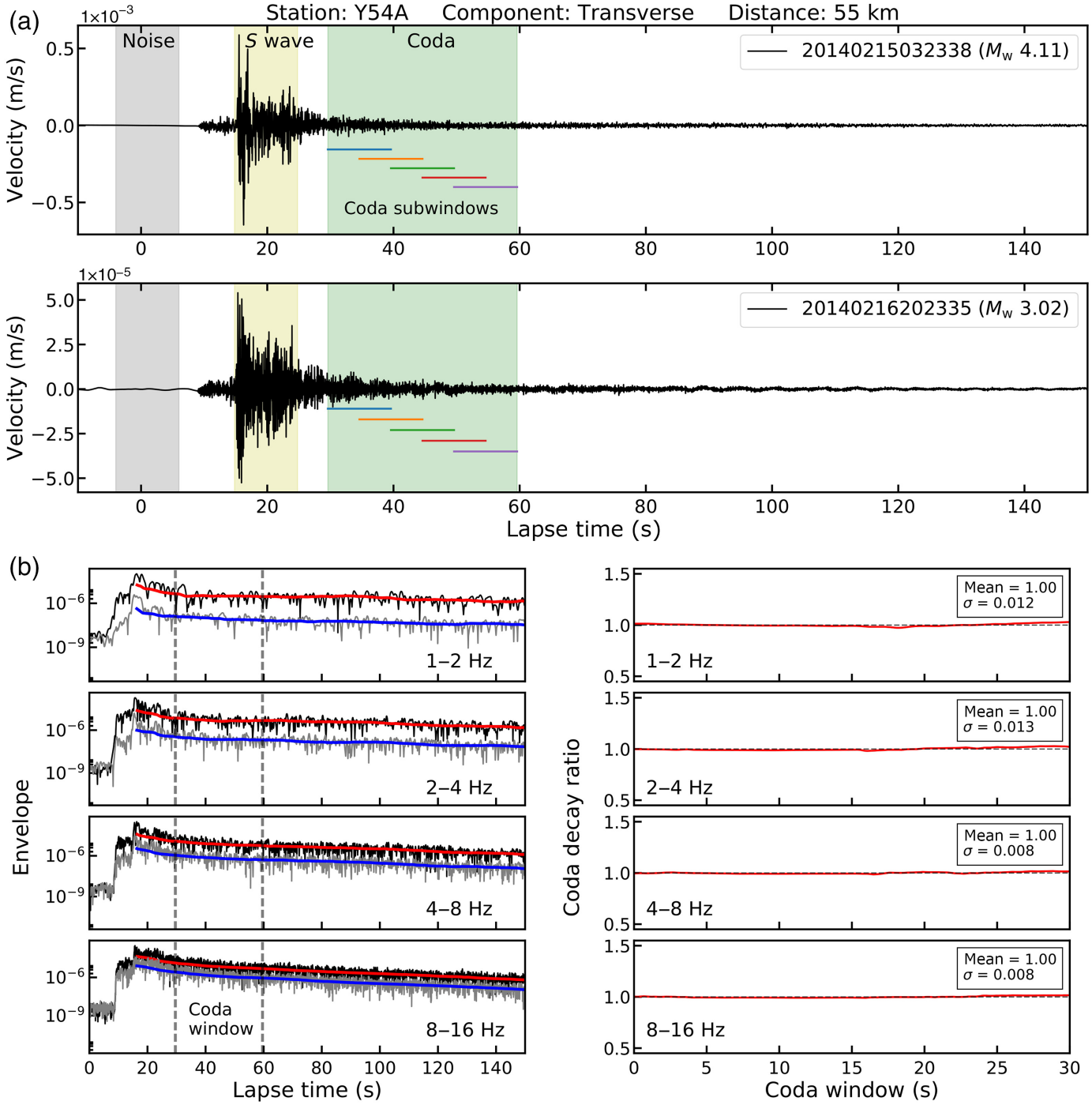

mainshock recorded at station Y55 are converted to ground velocity waveforms, using the transfer function in Seismic Analysis Code with four corner frequencies of 0.001–0.003 Hz and 10–20 Hz. Then, the ground velocity waveforms are low-pass-filtered with a corner frequency of 2 Hz (number of poles two, and number of passes two). The Central U.S. seismic velocity (CUS) model (Herrmann, 2013) and a modified version (M2) (Fig. 9a) are used in computing synthetic seismograms with the frequency–wavenumber (f–k) code of Zhu and Rivera (2002), and the SLU focal plane solutions are adopted in the calculation. The only difference between the CUS model

Figure 7. The mainshock and the aftershock recorded at station Y54A at an epicentral distance of 55 km. (a) The transverse-component velocity of the two events. The noise, direct *S* wave, and coda windows are denoted by shaded rectangles from left to right. Short horizontal bars mark the coda subwindows. (b) Comparison of coda decay rates for the two events. (Left) Narrowband original (black and gray) and smoothed envelopes of the seismograms shown in (a); (right) the normalized coda amplitude ratio across the entire coda window. The color version of this figure is available only in the electronic edition.

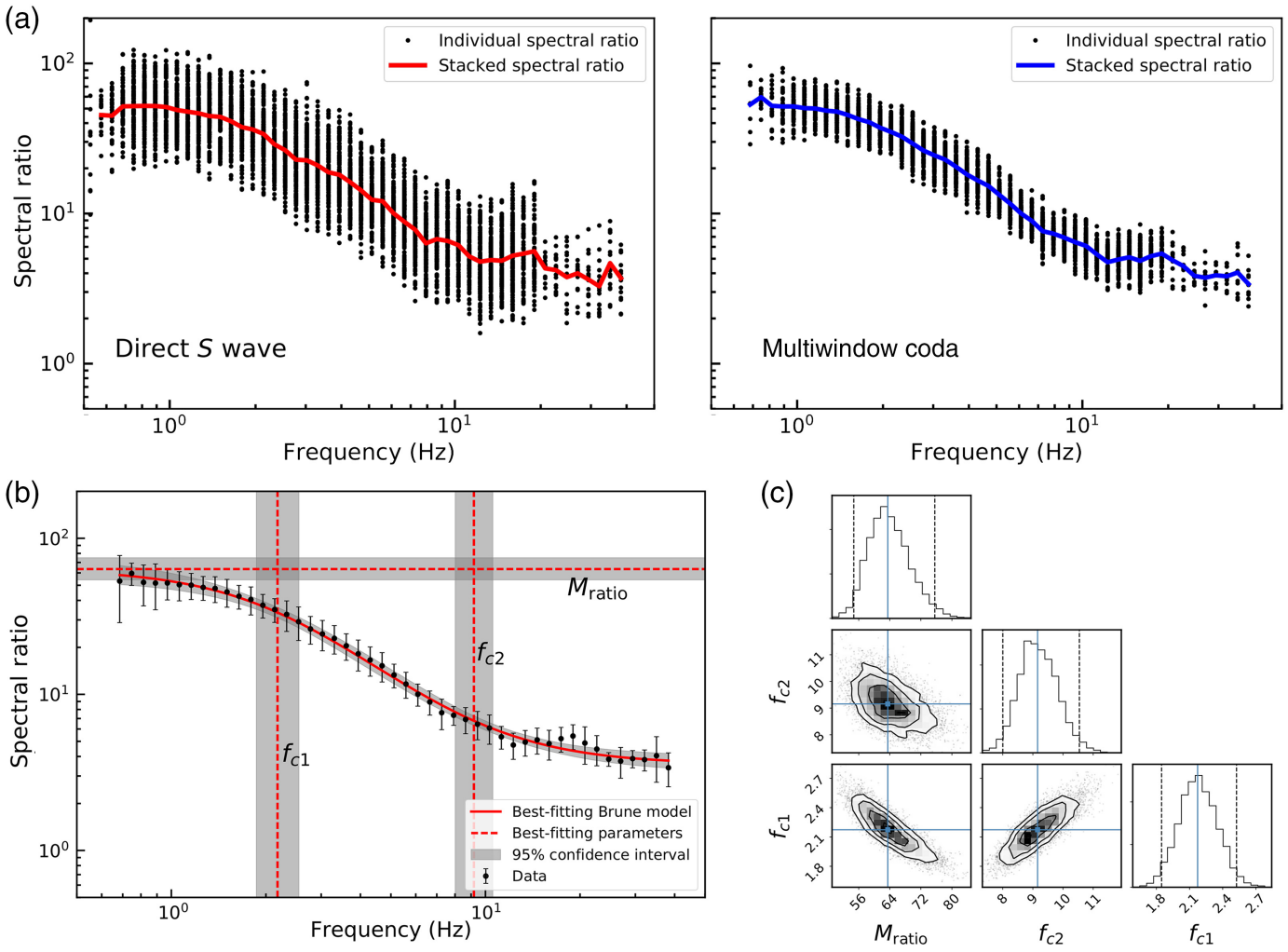

and M2 is in the shallowest 1 km, which contains a more gradual velocity increase in M2. Synthetics with the CUS and M2 models both match the observations well. However, the M2 model is preferred, because the synthetic waveform around 2 s after the *P* arrival better fits the observed seismogram of the mainshock at station TA.Y55 (Fig. 10). The negative and positive swing around 2 s after the *P* arrival is closely aligned for both the observed waveform and synthetic M2 model. In comparison, the observed waveform and synthetic CUS models do not match as well at 2 s after the *P* arrival, probably due to the sharp discontinuity modeled at a depth of 1.0 km. Therefore, the M2 model is adopted.

The phase near 2.0 s is probably the *sPL* phase, as proposed by Chong *et al.* (2010), which is related to the upgoing *S* wave and converted *P* waves in the surficial layer (Fig. 9b). In the case of a homogeneous half-space model, the upgoing *S* wave converts to a horizontally propagating *P* wave when the *S*-to-*P* reflection approaches the critical angle, and becomes the free surface *P* wave (Aki and Richards, 2002). However, for the case of a lower velocity layer above a half-space, the conversion of upgoing *S* wave leads to *sPhP* (similar to the *SsPmP*, Langston, 1996, as well as its multiples such as *sPhPPhP*). That is why Chong *et al.* (2010) named the wavetrains of free surface *P* wave as *sPhP* and later multiples as *sPL*, due to the complicated coupling nature. This phase arrives between the *P* and *S* waves (Fig. 11a), and is usually stronger on the radial component than the vertical component because of the nearly flat ray path of the *P* segment (Fig. 9b).

The differential time between *sPL* and *P* waves is sensitive to focal depth. In Figure 11, synthetics with focal depths of

Figure 8. The spectral ratios and corner-frequency estimates. (a) Individual (dot) and stacked (solid line) spectral ratios for (left) direct *S*-wave windows and (right) multiple coda windows measurement at all stations within 250 km; (b) the best-fitting Brune model (solid line). Dashed lines show the best estimates of model parameters (f_{c1}, f_{c2}, M_{ratio}). Shaded areas represent the 95% confidence intervals of the estimates; (c) the posterior distributions of the model parameters. Solid lines mark the best estimates, and vertical dashed lines outline the 95% confidence intervals. Diagonal panels show the posterior probability density functions of (top) M_{ratio}, (middle) f_{c2}, and (bottom) f_{c1}. Off-diagonal panels show the 2D projections of the posterior samples (gray dots) of the Markov chain Monte Carlo simulations. Contours represent 0.5, 1, 1.5, and 2 standard deviations. The color version of this figure is available only in the electronic edition.

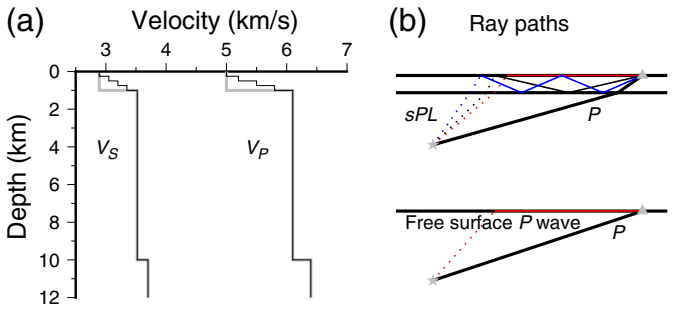

Figure 9. (a) V_P and V_S models. The Central U.S. seismic velocity (CUS) model (Herrmann, 2013) is indicated with gray thick lines, and a modified model (M2) with thin dark lines. (b) Ray path for (bottom) free surface *P* wave and (top) *sPL*. *sPL* forms from near-surface coupling effects, including free surface *P* wave, *sPhP*, *sPhPPhP*, and later multiples. The color version of this figure is available only in the electronic edition.

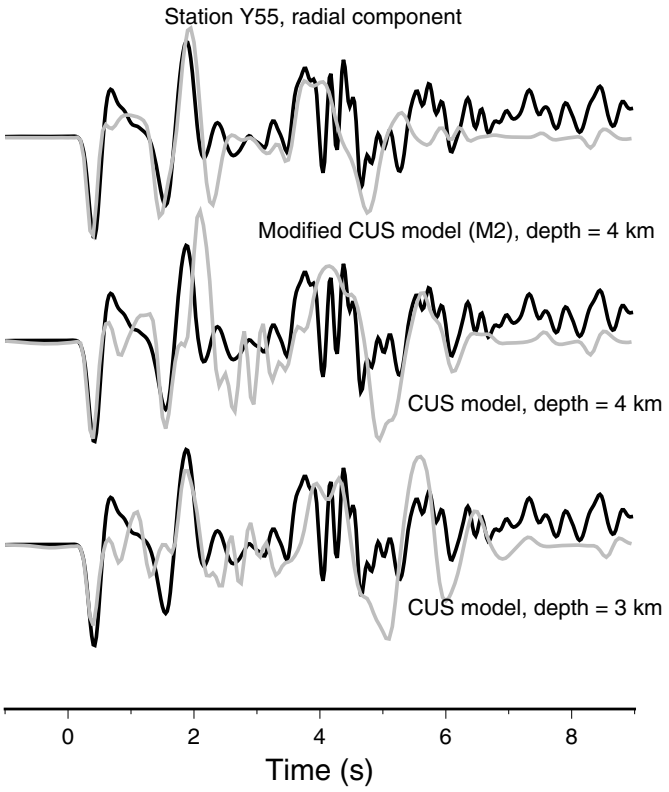

Figure 10. Comparison between observed (black) and synthetic (gray) waveforms of radial component for station Y55. The focal depth is indicated below each trace. Waveforms are normalized in amplitude.

3–5 km are compared to the observed radial component at station Y55. The timing difference between *sPL* and *P* is too large at a depth of 5 km, and too small at a depth of 3 km. Instead, for a depth of 4 km, the observed and synthetic waveforms have the best match. Moreover, the synthetic Rayleigh wave at a depth of 3 km seems to be stronger than in the observed waveform, and weaker at a depth of 5 km, again suggesting that a depth of 4 km is more probable. Using the Shen–Ritzwoller profile, the observed and synthetic waveforms have the best match at a depth of 3–4 km. The focal depth of 5–6 km from SLU and USGS-MT likely resulted from using longer period waves or stations at longer distances, where lateral variation of crustal structure may bias estimation of focal depth. For the M_w 3.0 aftershock (also low-pass-filtered with corner frequency of 2 Hz), the *sPL* arrival is also observable at station Y55, but less obvious due to lower SNR. The differential time between the *sPL* and *P* arrivals for the aftershock is close to that of the mainshock, suggesting a similar focal depth.

Discussion

We detected foreshocks and aftershocks around the 15 February 2014 M_w 4.1 earthquake near Edgefield, South Carolina. Starting with only two cataloged events (the M_w 4.1 mainshock and the M_w 3.0 aftershock) and iterating once with detections as new templates, the matched-filter technique yields 19 possible other events (Table 1). These include at least one previously undetected **M** 0.68 foreshock, as well as several aftershocks including the **M** 0.41 event (Fig. 4). The remaining six events with a threshold of 15 times the MAD can be easily identified on seismograms.

Approximately 95% of the detections have magnitudes less than 1. There is only 1 of the 19 detections with a magnitude between 1 and 3, with a magnitude of 1.92 (Fig. 6a). According to the G-R and the Båth's laws (Shcherbakov *et al.*, 2004), the M_w 4.1 event is supposed to be followed by one magnitude larger than 3, and about 100 events with magnitude larger than 1 (with the *b*-value of 1). Because the matched-filter method detected many events with magnitudes smaller than 1, it is reasonable to assume that if there were additional events with magnitudes greater than 1, they should have been detected. It thus seems that there are indeed very few events with magnitudes between 1 and 3 in this sequence, which is unusual for an event of this size at plate-boundary regions. However, this is not the only case when an M_w 4.0-type earthquake in the eastern United States has been followed by very few aftershocks. The 2012 M_w 4.0 Waterboro, Maine, earthquake is another example. Despite a dense temporary array being deployed in the days following the mainshock, only one aftershock was detected (Quiros *et al.*, 2015). The 2017 M_w 4.2 Delaware earthquake is another case in which there is a lack of larger magnitude aftershocks, with the only aftershocks having magnitudes less than M_w 2.0 (Kim *et al.*, 2018). Similarly, the 2003 M_w 4.3 double earthquake in the central Virginia seismic zone had no aftershocks detected, despite a month of aftershock monitoring by a temporary local network (Kim and Chapman, 2005).

The relative lack of background seismicity occurring near the mainshock and the relatively low number of aftershocks

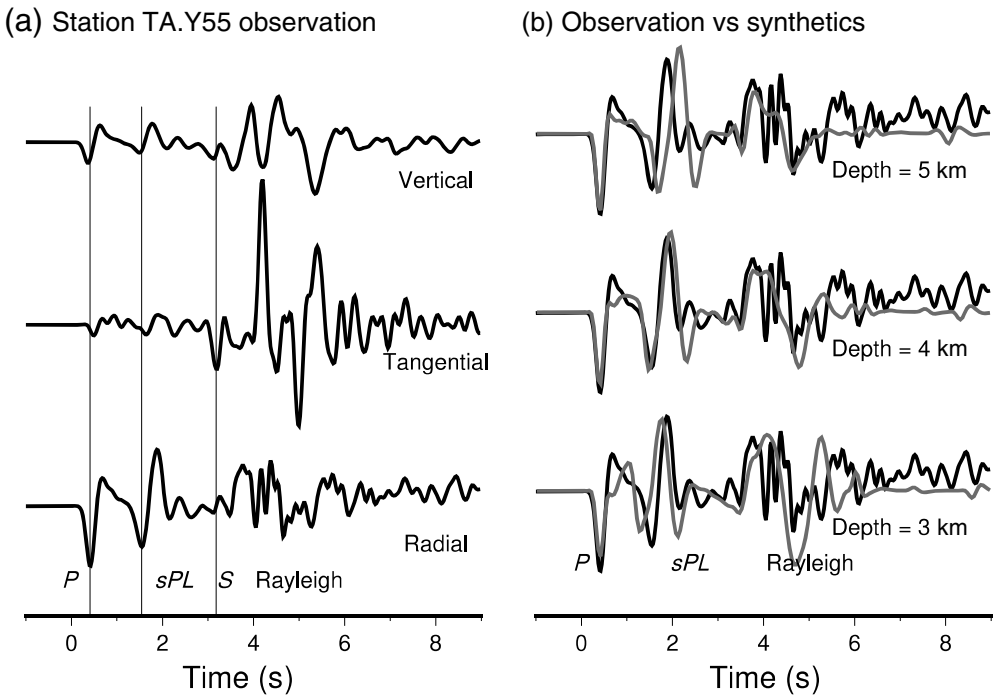

Figure 11. (a) Observed radial, tangential, and vertical component of waveforms at Y55 station. (b) Comparison between observed (black) and synthetic (gray) radial component for different depths. Low-pass filter is used with a corner frequency of 2 Hz, number of poles two, and number of passes two.

(and the associated low *a*-value in the G-R fit) suggest that, in general, earthquakes are difficult to nucleate in these regions, even during the aftershock time period. However, the nearby 1974 M_L 4.3 Clarks Hill Reservoir earthquake had prolific aftershocks, with several magnitude greater than 3, including the 8 October 1974 M_L 3 and 3 December 1974 M_L 3.6 earthquakes, as well as many aftershocks with magnitudes less than 2 (Talwani, 1976).

An alternative explanation is that most of the accumulated strain was released by the mainshock. Another interesting feature of this sequence is the low-calculated stress drops for the mainshock and its M_w 3.0 aftershock. A stress drop of 3.75 MPa for the M_w 4.1 earthquake and 4.44 MPa for the M_w 3.0 earthquake are less than expected for tectonic earthquakes in the central and eastern United States, which are typically on the order of ~10 MPa (e.g., Shi *et al.*, 1998; Viegas *et al.*, 2010; Boatwright and Seekins, 2011; Boyd *et al.*, 2017; Huang *et al.*, 2017; Wu and Chapman, 2017). The lower observed stress drops may be in part due to the depth of the earthquakes. The mainshock and its M_w 3.0 aftershock likely occurred at a depth shallower than initially estimated. Therefore, the energy released in the mainshock may be lower than previously thought. There is an observed increase in minimum stress drop with depth for eastern U.S. earthquakes, with the tendency for shallow earthquakes to exhibit lower stress drops (Long, 2019). The shallower depths may also account for the apparent deficit of aftershocks and triggered events from this earthquake. The 1974 M_L 4.3 Clarks Hill Reservoir earthquake had a similarly shallow depth of 1.5 km and a relatively low stress drop of 0.12–1.2 MPa (Bridges, 1975).

Historical records suggest on average an M_w 4.5 earthquake every 50 yr in the region of the Thurmond Reservoir, with a depth limit of 4 km due to hydrostatic loading (Long, 2009). The 2014 M_w 4.1 earthquake, situated in the region near the reservoir, supports these estimates. Its proximity to the Thurmond Reservoir, such as several other earthquakes in the region, indicates that there may be some causal effects from the Thurmond Reservoir. The 2014 M_w 4.1 earthquake may also have ruptured the nearby Modoc fault (Chowns, 1976), but whether the earthquake is related to this fault is unknown. Hence, further analysis of the regional stress field, geologic structures, reservoir-induced stress changes, and long-term earthquake behavior are needed to more definitively determine whether this seismicity is related to the reservoir.

Data and Resources

Seismic data used in this study were derived from the following sources: continuous seismic waveforms from the Z9 experiment network at https://ds.iris.edu/gmap/#network=Z9&starttime=2010-01-01&endtime=2014-12-31&planet=earth (last accessed August 2015); U.S. Geological Survey (USGS) moment-tensor solution at https://earthquake.usgs.gov/earthquakes/eventpage/se610610#moment-tensor (last accessed August 2015); the St. Louis University (SLU) solution for the M_w 4.1 mainshock and M_w 3.0 aftershock at http://www.eas.slu.edu/eqc/eqc_mt/MECH.NA/20140215032338/index.html and http://www.eas.slu.edu/eqc/eqc_mt/MECH.NA/20140216202335/index.html (last accessed December 2018); and the USGS "Did You Feel It?" Intensity Report at https://earthquake.usgs.gov/earthquakes/eventpage/se610610/dyfi/intensity (last accessed June 2019).

Acknowledgments

Seismic data utilized in this study are archived at the Incorporated Research Institutions for Seismology (IRIS) Data Management Center. The authors thank Tim Long, an anonymous reviewer, and Eastern-Section Editor Oliver Boyd for their valuable comments. Clara Daniels acknowledges financial support from the Southern California Earthquake Center's (SCEC's) Summer Internship

Program. Clara Daniels and Zhigang Peng are supported by National Science Foundation (NSF) Grant Number EAR-1818161 and U.S. Geological Survey (USGS) National Earthquake Hazards Reduction Program (NEHRP) Grant Number G15AP00070.

References

Aki, K., and P. Richards (2002). *Quantitative Seismology*, University Science Books, Sausalito, California.

Boatwright, J. (1980). A spectral theory for circular seismic sources: Simple estimates of source duration, dynamic stress drop, and radiated energy, *Bull. Seismol. Soc. Am.* **70,** 1–28.

Boatwright, J., and L. Seekins (2011). Regional spectral analysis of three moderate earthquakes in northeastern North America, *Bull. Seismol. Soc. Am.* **101,** 1769–1782.

Bollinger, G. A., A. C. Johnston, P. Talwani, L. T. Long, K. M. Sedlock, M. S. Sibol, and M. C. Chapman (1991). Seismicity of the southeastern United States 1698 to 1986, in *Neotectonics of North America*, D. B. Slemmons, E. R. Engdahl, M. D. Zoback, and D. D. Blackwell (Editors), Decade Map, Vol. 1, Geological Society of America, Boulder, Colorado, 291–308.

Boyd, O. S., D. E. McNamara, S. Hartzell, and G. Choy (2017). Influence of lithostatic stress on earthquake stress drops in North America, *Bull. Seismol. Soc. Am.* **107,** no. 2, doi: 10.1785/0120160219.

Bridges, S. (1975). Evaluation of stress drop of the August 2, 1974 Georgia-South Carolina earthquake and aftershock sequence, *Master's Thesis*, Georgia Institute of Technology, Atlanta, Georgia, 103 pp.

Brune, J. (1970). Tectonic stress and the spectra of seismic shear waves from earthquakes, *J. Geophys. Res.* **75,** no. 26, 4997–5009.

Brune, J. N. (1971). Correction, *J. Geophys. Res.* **76,** 5002.

Chong, J. J., S. D. Ni, and X. F. Zeng (2010). sPL, an effective seismic phase for determining focal depth at near distances, *Chinese J. Geophys.* **53,** no. 11, 2620–2630, doi: 10.3969/j.issn.0001-5733.2010.11.010 (in Chinese).

Chowns, T. M. (1976). *Introduction, Stratigraphy, Structure, and Seismicity in Slate Belt Rocks along the Savannah River*, Guidebook 16, Georgia Geological Society, Atlanta, Georgia, 2–8.

Costain, J. (2008). Intraplate seismicity, hydroseismicity, and predictions in hindsight, *Seismol. Res. Lett.* **79,** no. 4, 578–589, doi: 10.1785/gssrl.79.4.578.

Eshelby, J. D. (1957). The determination of the elastic field of an ellipsoidal inclusion and related problems, *Proc. Math. Phys. Sci.* **241,** 376–396, doi: 10.1785/0120020217.

Fischer, K., R. Hawman, and L. S. Wagner (2010). *Southeastern Suture of the Appalachian Margin Experiment*, International Federation of Digital Seismograph Networks, Other/Seismic Network, doi: 10.7914/SN/Z9_2010.

Frankel, A. (2015). Decay of S-wave amplitudes with distance from earthquakes in the Charlevoix, Quebec area: Effects of radiation pattern and directivity, *Bull Seismol. Soc. Am.* **105,** 850–857.

Guinn, S. A. (1977). Earthquake focal mechanisms in the southeastern United States, *Master's Thesis*, Georgia Institute of Technology, Atlanta, Georgia, 150 pp.

Gupta, H. K., B. K. Rastogi, and H. Narain (1972). Some discriminatory characteristics of earthquakes near the Kariba, Kremasta, and Koyna artificial lakes, *Bull. Seismol. Soc. Am.* **62,** no. 2, 493–507.

Herrmann, R. B. (2013). Computer programs in seismology: An evolving tool for instruction and research, *Seismol. Res. Lett.* **84,** no. 6, 1081–1088, doi: 10.1785/0220110096.

Hopper, E., K. M. Fischer, L. S. Wagner, and R. B. Hawman (2017). Reconstructing the end of the Appalachian Orogeny, *Geology* **45,** 15–18, doi: 10.1130/G38453.1.

Huang, Y., W. L. Ellsworth, and G. C. Beroza (2017). Stress drops of induced and tectonic earthquakes in the central United States are indistinguishable, *Sci. Adv.* **3,** no. 8, e1700772.

Imanishi, K., and W. L. Ellsworth (2006). Source scaling relationships of microearthquakes at Parkfield, CA, determined using the SAFOD Pilot Hole seismic array, in *Earthquakes: Radiated Energy and the Physics of Faulting*, R. Abercrombie, A. McGarr, G. D. Toro, and H. Kanamori (Editors), American Geophysical Union, Washington, D.C., 81–90.

Johnston, G. L. (1980). A seismic spectral discriminant for reservoir induced earthquake in the southeastern United States, *Master's Thesis*, Georgia Institute of Technology, Atlanta, Georgia, 117 pp.

Kim, W., and M. C. Chapman (2005). The 9 December 2003 central Virginia earthquake sequence: A compound earthquake in the central Virginia seismic zone, *Bull. Seismol. Soc. Am.* **95,** 2428–2445.

Kim, W., M. Gold, J. Ramsay, A. Meltzer, D. Wunsch, S. Baxter, V. Lekic, P. Goodling, K. Goodling, L. Wagner, *et al.* (2018). The M_w 4.2 Delaware earthquake of 30 November 2017, *Seismol. Res. Lett.* **89,** no. 6, 2447–2460.

Langston, C. (1996). The *SsPmp* phase in regional wave propagation, *Bull. Seismol. Soc. Am.* **86,** 133–143.

Long, L. T. (2009). The Central Georgia Seismicity, in *Georgia Geological Society Guidebook*, Vol. 29, 65–70.

Long, L. T. (2019). The mechanics of natural and induced shallow seismicity: A review and speculation based on studies of eastern U.S. earthquakes, *Bull. Seismol. Soc. Am.* **109,** no. 1, 336–347, doi: 10.1785/0120180310.

Marion, G., and L. T. Long (1980). Microearthquake spectra in the southeastern United States, *Bull. Seismol. Soc. Am.* **70,** no. 4, 1037–1054.

Mayeda, K., L. Malagnini, and W. R. Walter (2007). A new spectral ratio method using narrow band coda envelopes: Evidence for nonself-similarity in the Hector Mine sequence, *Geophys. Res. Lett.* **34,** L11303, doi: 10.1029/2007GL030041.

Meng, X., Z. Peng, and J. Hardebeck (2013). Seismicity around Parkfield correlates with static shear stress changes following the 2003 Mw 6.5 San Simeon earthquake, *J. Geophys. Res.* **118,** 3576–3591, doi: 10.1002/jgrb.50271.

Parker, E. H., R. B. Hawman, K. M. Fischer, and L. S. Wagner (2013). Crustal evolution across the southern Appalachians: Initial results from the SESAME broadband array, *Geophys. Res. Lett.* **40,** 3852–3857, doi: 10.1002/grl.50761.

Parker, E. H., R. B. Hawman, K. M. Fischer, and L. S. Wagner (2016). Estimating crustal thickness using SsPmp in regions covered by low-velocity sediments: Imaging the Moho beneath the Southeastern Suture of the Appalachian Margin Experiment (SESAME) array, SE Atlantic Coastal Plain, *Geophys. Res. Lett.* **43,** 9627–9635.

Peng, Z., and P. Zhao (2009). Migration of early aftershocks following the 2004 Parkfield earthquake, *Nat. Geosci.* **2,** doi: 10.1038/ngeo697.

Prieto, G. A., R. L. Parker, and F. L. Vernon (2009). A Fortran 90 library for multitaper spectrum analysis, *Comput. Geosci.* **35,** 1701–1710.

Quiros, D., A. Cabolova, D. Brown, C. Chen, J. Ebel, and J. Starr (2015). Aftershock Imaging with Dense Arrays (AIDA) following the M_w 4.0 Waterboro earthquake of 16 October 2012 Maine, U.S.A., *Seismol. Res. Lett.* **86,** no. 3, 1032–1039.

Salvatier, J., T. V. Wiecki, and C. Fonnesbeck (2016). Probabilistic programming in Python using PyMC3, *Peer J. Comput. Sci.* **2,** e55, doi: 10.7717/peerj-cs.55.

Shcherbakov, R., D. L. Turcotte, and J. B. Rundle (2004). A generalized Omori's law for earthquake aftershock decay, *J. Geophys. Res.* **31,** L11613, doi: 10.1029/2004GL019808.

Shelly, D. R., G. C. Beroza, and S. Ide (2007). Non-volcanic tremor and low frequency earthquake swarms, *Nature* **446,** 305–307, doi: 10.1038/nature05666.

Shi, J., W. Y. Kim, and P. Richards (1998). The corner frequency and stress drops of intraplate earthquakes in the northeastern United States, *Bull. Seismol. Soc. Am.* **88,** 531–542.

Somei, K., K. Asano, T. Iwata, and K. Miyakoshi (2014). Source scaling of inland crustal earthquake sequences in Japan using the S-wave coda spectral ratio method, *Pure Appl. Geophys.* **171,** no. 10, 2747–2766.

Talwani, P. (1976). Earthquakes associated with the Clarks Hill Reservoir, South Carolina—A case of induced seismicity, *Eng. Geol.* **20,** 239–253.

Viegas, G. (2012). Source parameters of the 16 July 2010 M_w 3.4 Germantown, Maryland, earthquake, *Seismol. Res. Lett.* **83,** 933–944, doi: 10.1785/0220110056.

Viegas, G., R. Abercrombie, and W. Y. Kim (2010). The 2002 M5 Au Sable Forks, NY, earthquake sequence: Source scaling relationships and energy budget, *J. Geophys. Res.* **115,** no. B07310, doi: 10.1029/2009JB006799.

Wu, Q., and M. C. Chapman (2017). Stress-drop estimates and source scaling of the 2011 Mineral, Virginia, mainshock and aftershocks, *Bull. Seismol. Soc. Am.* **107,** 2703–2720.

Wu, Q., M. C. Chapman, J. N. Beale, and S. Shamsalsadati (2016). Near-source geometrical spreading in the central Virginia seismic zone determined from the aftershocks of the 2011 Mineral, Virginia, earthquake, *Bull. Seismol. Soc. Am.* **106,** 943–955.

Wu, Q., M. C. Chapman, and X. Chen (2018). Stress-drop variations of induced earthquakes in Oklahoma, *Bull. Seismol. Soc. Am.* **108,** no. 3A, 1107–1123.

Zhu, L., and L. A. Rivera (2002). A note on the dynamic and static displacements from a point source in multilayered media, *Geophys. J. Int.* **148,** no. 3, 619–627.

Manuscript received 5 February 2019
Published online 6 November 2019